TIM-22-00315R1

On the use of an Equivalent Currents-based Technique to improve Electromagnetic Imaging

Yuri Álvarez López and Fernando Las-Heras, *Senior Member, IEEE*

***Abstract*—Accurate imaging from scattered field measurements is one of the main research topics in the field of Non-Destructive Testing. Different methodologies for inverse scattering have been developed, ranging from backpropagation techniques to full-wave inversion methods. While far field approaches are valid for the majority of the imaging systems, there are some scenarios where these approaches do not provide accurate modeling of the field radiated by the antennas of the imaging system. This results in some kind of distortion in the resulting output microwave images. To address this issue, proper characterization and modeling of the fields radiated by the antennas is required.**

This contribution proposes the use of an equivalent currents-based technique to characterize the transmitting and receiving antennas of the imaging sensor. The goal is to calculate accurately the field radiated by these antennas within the imaging domain, using it in the backpropagation algorithm. The methodology described in this contribution is supported by measurements for monostatic and multistatic configurations.

***Index Terms*—Microwave imaging, Delay-and-Sum, Sources Reconstruction Method, antenna measurement.**

I. Introduction

ELECTROMAGNETIC imaging techniques have been widely introduced in different application areas where non-destructive testing systems are required. Examples of microwave imaging systems can be found in security screening applications [1]-[3], Ground Penetrating Radar (GPR) [4], or infrastructure inspection [5].

Inverse scattering and imaging systems usually require a calibration stage to equalize the frequency response of the different components of these systems (cables, connectors, antennas) [6]. This is of special relevance in Ultra Wide Band (UWB) systems, where antenna parameters like the radiation pattern, gain, and directivity usually exhibit a large variation along the frequency band. In this sense, it can be cited the analysis presented in [7] about the impact of the antenna gain pattern on Synthetic Aperture Radar (SAR) imaging.

Several equalization methods have been developed to compensate for the amplitude of the frequency response of the radiofrequency components of the imaging system. For example, [8] presents an equalization technique where the reflectivity image is calculated for each individual frequency, then normalizing each one with respect to its maximum.

The displacement of the phase center of the antenna within the working frequency band has an impact on the focusing of the recovered images from scattered field measurements. In this sense, different techniques have been proposed to compensate for the displacement of the phase center. For example, a group delay model is presented in [9]. Another approach is tested in [10], based on splitting the whole frequency band into narrower bands and considering constant the position of the phase center within each sub-band.

From the review of the state-of-the-art, it can be concluded that two are the main approaches followed to compensate for the distortion introduced by the radiofrequency devices in UWB imaging systems. One is splitting the frequency band into sub-bands where the transfer function of these components and devices does not change significantly within such sub-bands. The other requires a complete characterization of the frequency response of these radiofrequency components to correct the distortion.

The fields radiated by an antenna can be calculated at any point of the space if an accurate electromagnetic model of the antenna is provided. This model can be derived from simulations, which will require creating a detailed model of the antenna in an electromagnetics simulation software. Another possibility is the measurement of the field radiated by the antenna, then using the measured field to retrieve an equivalent electromagnetic model of the antenna. This model can be later used to calculate the field radiated by the antenna at the desired points. This technique has been widely used for near field-to-far field transformation (NF-FF) as well as for antenna diagnostics [11]-[13].

Different approaches to model the electromagnetic fields radiated by the imaging sensors (namely the transmitting (Tx) and receiving (Rx) antennas) have been proposed in the literature. For example, [14] introduces a quantitative model of the antennas that does not require an additional calibration process. [15] makes use of two different incident field models: a two-dimensional (2D) line-source and an incident field obtained from full-wave three-dimensional (3D) simulation of the tomographic imaging system. In [16] the authors make use

Y. Álvarez and F. Las-Heras are with the Department of Electrical, Electronics, Communications and Systems of the University of Oviedo. Edificio Polivalente, Mod. 8, Campus Universitario de Gijón. 33203, Gijón (Spain). Email: {alvarezyuri, flasheras}@uniovi.es.

This work was supported in part by the Principado de Asturias / FICYT under grant “Ayudas para grupos de investigación de organismos del Principado de Asturias durante el período 2021-2023”, reference AYUD/2021/51706; and by the Ministry of Science and Innovation of Spain under project META-IMAGER, and under project RTI2018-095825-B-I00 (“Millihand”).

Corresponding author: Y. Álvarez López.

of the Sources Reconstruction Method (SRM) to model the incident field radiated by the transmitting antenna of the imaging system.

This contribution improves the methodology presented in [16] through the characterization of either the Tx and Rx antennas of the microwave imaging system, also extending the methodology to 3D imaging examples. The imaging algorithm to be considered is the Delay-and-Sum (DAS).

II. Characterization of the Imaging Sensor

Delay-and-Sum is a well-known inverse scattering and imaging technique based on the backpropagation of the scattered field from the measurement domain to the imaging domain [17]. The DAS algorithm has been widely used not only in electromagnetics but also in seismic applications [18] and acoustics [19].

Given the scattered field $\vec{E}_{scatt}$ acquired in a set of N observation points ($\vec{r}_{obs}$) and in a frequency band discretized into M_f frequencies, the reflectivity in a point belonging to the imaging domain, $\rho(\vec{r}')$, is given by (1):

$$\rho(\vec{r}') = \sum_{m=1}^{M_f} \sum_{n=1}^{N} \left\{ \vec{E}_{scatt}\left(\vec{r}_{obs,n}, f_m\right) e^{+j2k_{0,m}R_n} \right\}, \quad (1)$$

where $k_{0,m}$ is the wavenumber at the m-th frequency, and R_n is the Euclidean distance between the n-th acquisition point of the scattered field, $\vec{r}_{obs,n}$, and the imaging position $\vec{r}'$. In Eq. (1) a monostatic configuration is considered, that is, the Tx and Rx antennas are located at the same position, $\vec{r}_{obs}$.

In the case of multistatic configurations, i.e., the Tx and Rx antennas are located in different positions, Eq. (1) is updated as follows (2):

$$\rho(\vec{r}') = \sum_{m=1}^{M_f} \sum_{n=1}^{N} \left\{ \vec{E}_{scatt}\left(\vec{r}_{obs,n}, f_m\right) e^{+jk_{0,m}(R_{Tx}+R_{Rx,n})} \right\}, \quad (2)$$

where R_{Tx} is the Euclidean distance between the position of the Tx and the imaging position $\vec{r}'$, and $R_{Rx,n}$ is the Euclidean distance between the n-th position of the Rx and the imaging position $\vec{r}'$. Note that, in this multistatic configuration, the Tx is placed at a fixed position while the Rx is moved along N receiving positions to collect the scattered field.

As noticed in Eqs. (1) and (2), the DAS algorithm is based on an approach that only considers the phase term of a spherical wave (e^{-jk_0R}). While for the majority of the imaging applications described in the literature this approach is accurate enough, in some scenarios the impact of the antenna radiation pattern of the Tx and Rx antennas in the microwave imaging results is not negligible. Furthermore, the phase difference between the spherical wave approach and the complex radiation pattern of the Tx and Rx antennas requires a calibration stage to compensate for the shifting in the position of the imaged objects.

To illustrate this, a two-dimensional (2D) simulation-based example is presented next. A full-wave Method-of-Moments code has been used for the simulation of the incident and scattered fields in a frequency band ranging from 12 GHz to 18 GHz (this frequency band has been chosen to make it coincident with the one used in the measurements of Section IV). In Fig. 1 (a), the Tx is a point source, whereas in Fig. 1 (b) and Fig. 1 (c) an Open-Ended Waveguide (OEWG) antenna is considered. The width of the aperture of the OEWG is 3 cm (D_{OEWG} = 3 cm), so the far field (FF) distance for this antenna is: $r_{FF} = 2(D_{OEWG})^2 / \lambda$ = 7.2 cm at 12 GHz, and 10.8 cm at 18 GHz. Besides, if the criterion $r_{FF} >> \lambda$ is also taken into account, then, r_{FF} > 25 cm at 12 GHz.

Even though the targets are located in the FF region of the OEWG antenna, differences in the amplitude of the field illuminating the targets are observed at f = 12 GHz (Fig. 1 (b)) and at f = 18 GHz (Fig. 1 (c)).

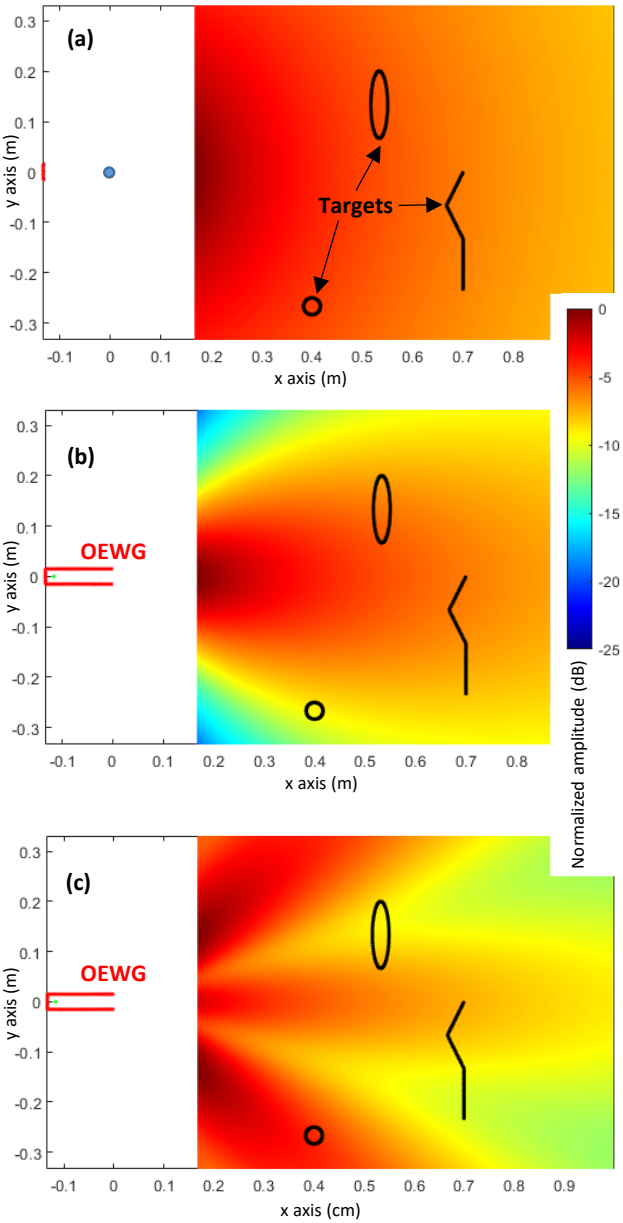

Fig. 1. Amplitude of the electric field radiated by (a) a point source, (b) an OEWG antenna at f = 12 GHz, and (c) an OEWG antenna at f = 18 GHz. Several metallic targets considered for further assessment of the imaging algorithms are depicted.

The differences between the field radiated by the point source Tx and the OEWG are also noticed in the phase. Fig. 2 (a) shows the phase distribution of the point source. The phase difference between the field radiated by a point source and the OEWG antenna is depicted in Fig. 2 (b) (f = 12 GHz) and in Fig. 2 (c) (f = 18 GHz). For the lowest frequency, the phase difference is less than 10 degrees within the area where the targets are located. However, for the highest frequency, the phase difference exceeds +/-90º. The impact of this phase error in the DAS imaging algorithm will be illustrated in Section III.B.

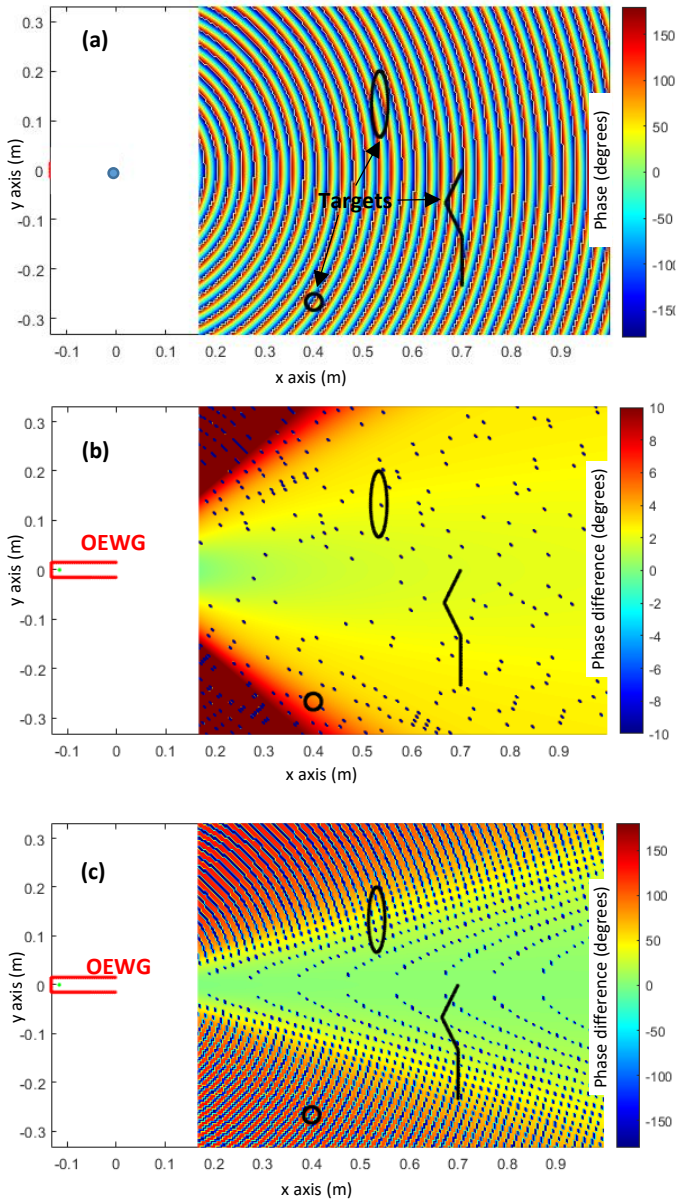

Fig. 2. (a) Phase of the electric field radiated by a point source. (b) Phase difference between the field radiated by a point source and an OEWG antenna at f = 12 GHz. (c) Phase difference between the field radiated by a point source and an OEWG antenna at f = 18 GHz.

III. Methodology

This section describes the proposed methodology that takes into account the fields radiated by the Tx and Rx antennas in the DAS imaging algorithm. First, the method implemented to characterize the Tx and Rx antennas is described in Section III.A. Next, the modified DAS algorithm is outlined in Section III.B.

A. Electromagnetic Equivalent Problem and the SRM

The electromagnetic Equivalence Principle states that, given an arbitrary distribution of electromagnetic sources enclosed within a surface S_c, then, it is possible to find an equivalent currents distribution, $\vec{J}_{eq}$ and $\vec{M}_{eq}$, defined on the surface S_c, that radiates the same field as the original sources outside the surface S_c [20]. Thus, if one can recover the equivalent currents modeling the radiation of the Antenna Under Test (AUT), it is possible to assess accurately the field radiated by the AUT at any point of the space outside the equivalent currents domain, S_c.

The equivalent currents distribution can be reconstructed from the measurement of the field radiated by the AUT on a closed surface, $\vec{E}_{acq}(\vec{r})$, as shown in Fig. 3 (a) (e.g. a circumference in 2D, or a sphere in 3D). The equivalent electric and magnetic currents are related to the field radiated by the AUT by means of the integral equations (3)-(5) [11]:

$$\vec{E}_{acq}(\vec{r}) = \vec{E}_J(\vec{r}) + \vec{E}_M(\vec{r}), \tag{3}$$

$$\vec{E}_J(\vec{r}) = -\frac{j\eta}{4\pi k_0}\int_{S_c}\left\{k_0^2(1+\nabla\nabla\cdot)\left(\vec{J}_{eq}(\vec{r}_c)\frac{e^{-jk_0R}}{R}\right)\right\}dS_c, \tag{4}$$

$$\vec{E}_M(\vec{r}) = -\frac{1}{4\pi}\nabla\times\int_{S_c}\vec{M}_{eq}(\vec{r}_c)\frac{e^{-jk_0R}}{R}dS_c. \tag{5}$$

In (4),(5) R is the Euclidean distance between the acquisition point $\vec{r}$ and the point of the equivalent currents domain $\vec{r}_c$. S_c denotes the surface where the equivalent currents, $\vec{J}_{eq}$ and $\vec{M}_{eq}$ (the unknowns in Eqs. (4)-(5)), are reconstructed.

Different methods have been developed to solve these integral equations [11]-[13]. In this contribution, the one presented in [11], based on the Conjugate Gradient, is considered.

Note that, in the case of NF-FF transformation for antenna measurement [11]-[13], the closed surface where the field radiated by the AUT is acquired is located in the NF region of the AUT. Nevertheless, the equivalent currents that characterize the AUT can be also reconstructed even if the acquisition surface is located in the FF region.

Two other issues must be taken into account to obtain an accurate equivalent currents-based model of the AUT:

i) As a rule-of-thumb, the acquisition domain must be large enough so that most of the power radiated by the AUT is captured. That is why, in the case of directive antennas, like those ones used in Section IV (Vivaldi, Standard Gain Horn), a finite planar acquisition domain can be used.

ii) The measurement of the field radiated by the antennas

should be performed in obstacle-free environments, to minimize the impact of reflections and multipath contributions.

Following the example of the imaging system presented in Section II, where the Tx/Rx antenna is an OEWG, Fig. 3 (a) shows the definition of the radiated field acquisition domain (a 33 cm radius circle, dashed red line) and the equivalent currents domain (rectangular domain S_c, dashed black line). The field radiated by the AUT, and the field radiated by the equivalent currents reconstructed from $\vec{E}_{acq}$, will be the same outside the reconstruction domain (S_c). In this example, the radiated field is acquired in the FF region of the AUT, as 33 cm > r_{FF} (if the criterion $r_{FF} >> \lambda$ is considered, then, r_{FF} = 25 cm at 12 GHz).

The previous methodology to characterize the AUT is summarized in the first four steps of the flowchart of Fig. 4.

B. Modified backpropagation method

The equivalent currents model of the Tx and Rx antennas of the imaging system can be used to calculate the field radiated by these antennas in the imaging domain. These fields will be introduced in the DAS method described in Section II. The goal is to replace the term e^{-jk_0R}, which corresponds to the FF approach of the phase, with the actual phase distribution of the field radiated by the antenna in the imaging domain $\vec{r}'$ (Fig. 3 (b)). The field radiated by the antenna (characterized through the equivalent currents $\vec{J}_{eq}$, $\vec{M}_{eq}$) in the imaging domain is calculated using the same integral equations (3)-(5). For the sake of clarity, the equations for the Tx antenna (6)-(8) are provided next (the same for the Rx antenna).

$$\vec{E}_{rad,Tx}(\vec{r}') = \vec{E}^{Tx}_{rad,J}(\vec{r}') + \vec{E}^{Tx}_{rad,M}(\vec{r}'), \quad (6)$$

$$\vec{E}^{Tx}_{rad,J}(\vec{r}') = -\frac{j\eta}{4\pi k_0}\int_{S_c}\left\{k_0^2(1+\nabla\nabla\cdot)\left(\vec{J}_{eq}(\vec{r}_c)\frac{e^{-jk_0R}}{R}\right)\right\}dS_c, \quad (7)$$

$$\vec{E}^{Tx}_{rad,M}(\vec{r}') = -\frac{1}{4\pi}\nabla\times\int_{S_c}\vec{M}_{eq}(\vec{r}_c)\frac{e^{-jk_0R}}{R}dS_c. \quad (8)$$

Note that if a point source was considered in Eqs. (6)-(8), these equations could be simplified, and the phase of the field in the imaging domain would be given by e^{-jk_0R}, which is the FF approach.

Thus, Eq. (2) of the DAS method is updated as follows:

$$\rho(\vec{r}') = \sum_{m=1}^{M_f}\sum_{n=1}^{N}\left\{\vec{E}_{scatt}(\vec{r}_{obs,n}, f_m)\cdot e^{+j\langle(\vec{E}_{rad,Tx}(\vec{r}',f_m))^*\rangle+\langle(\vec{E}_{rad,Rx}(\vec{r}',f_m))^*\rangle}\right\} \quad (9)$$

where the terms $\langle\vec{E}_{rad,Tx}(\vec{r}', f_m)\rangle$ and $\langle\vec{E}_{rad,Rx}(\vec{r}', f_m)\rangle$ are the phase of the field radiated by the equivalent currents that characterize the Tx and Rx antennas, respectively, calculated at the point $\vec{r}'$. In the case of a monostatic configuration, $\vec{E}_{rad,Tx} = \vec{E}_{rad,Rx}$.

The last three steps of the flowchart shown in Fig. 4 illustrate the proposed methodology to include the complex radiation pattern of the Tx and Rx antennas in the DAS algorithm. In brief, it consists of acquiring the field scattered by the targets located within the investigation domain $\vec{r}'$ at each *n*-th position of the observation domain, $\vec{E}_{scatt}(\vec{r}_{obs,n}, f_m)$, as illustrated in Fig. 3 (b). Next, Eq. (9) is applied to recover the reflectivity $\rho(\vec{r}')$ in all the points of the investigation domain.

It must be pointed out that the calculation of $\vec{E}_{rad,Tx}$ (and, if needed, $\vec{E}_{rad,Rx}$) in all the points of the investigation domain $\vec{r}'$ is done once. That is, there is no need to calculate these fields again every time a new target is placed in the imaging system. Only if the observation domain ($\vec{r}_{obs}$) and/or the imaging domain ($\vec{r}'$) are modified, then, the fields radiated by the Tx and Rx antennas need to be recalculated.

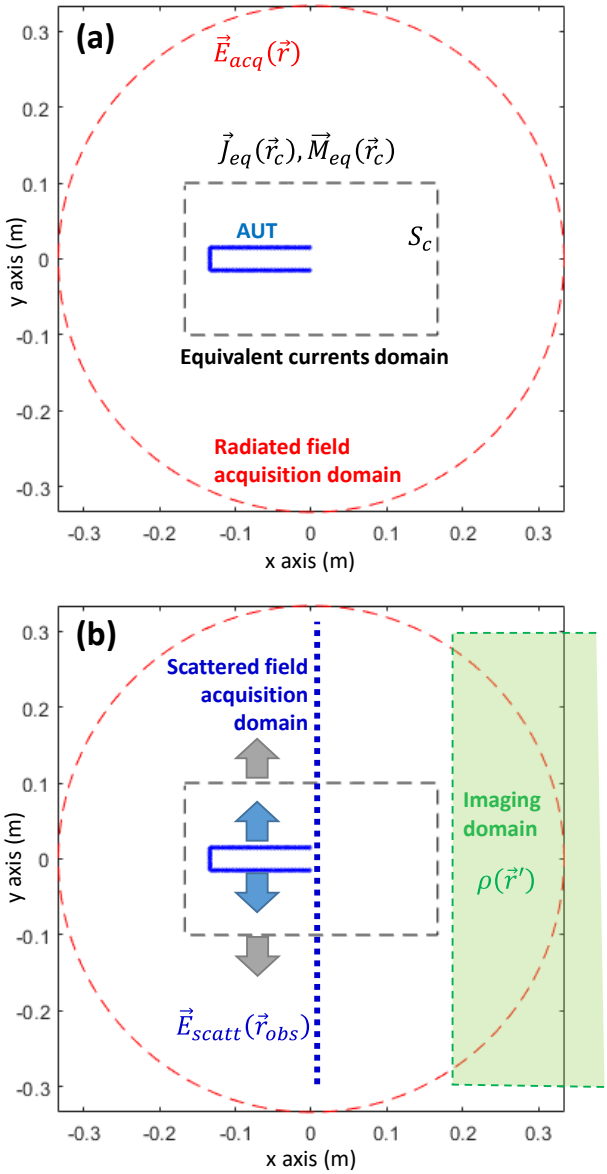

Fig. 3. (a) Scheme of the inverse radiation problem to characterize the AUT. (b) Scheme of the inverse scattering problem, indicating the scattered field acquisition domain and the imaging domain.

To assess the proposed modified backpropagation method, a simulation-based example is presented next. The monostatic configuration is the same as in Fig. 1: the Tx/Rx antenna is also an OEWG working in the 12 GHz to 18 GHz frequency band. The field scattered by the three metallic objects located in the imaging domain is collected along a linear domain ranging from y = - 30 cm ($\vec{r}_{obs,1}$) to y = +30 cm ($\vec{r}_{obs,N}$), discretized every λ/2 at 18 GHz.

First, the reflectivity in the imaging domain is recovered by applying the DAS backpropagation method based on Eq. (1). Results depicted in Fig. 5 (a) show that the imaged targets (i.e. the areas corresponding to the highest reflectivity values) are shifted along x axis with respect to their true position. This shifting happens because the spherical wave approach of the DAS does not properly model the phase of the field radiated by the OEWG antenna within the imaging domain, as shown in Fig. 2.

Next, an equivalent currents distribution that characterizes the Tx/Rx OEWG is calculated following the methodology described in Section II.B. From these equivalent currents, the fields radiated by the OEWG at each point of the imaging domain ($\vec{r}'$), and for every position of the observation domain ($\vec{r}_{obs,n}$), are calculated.

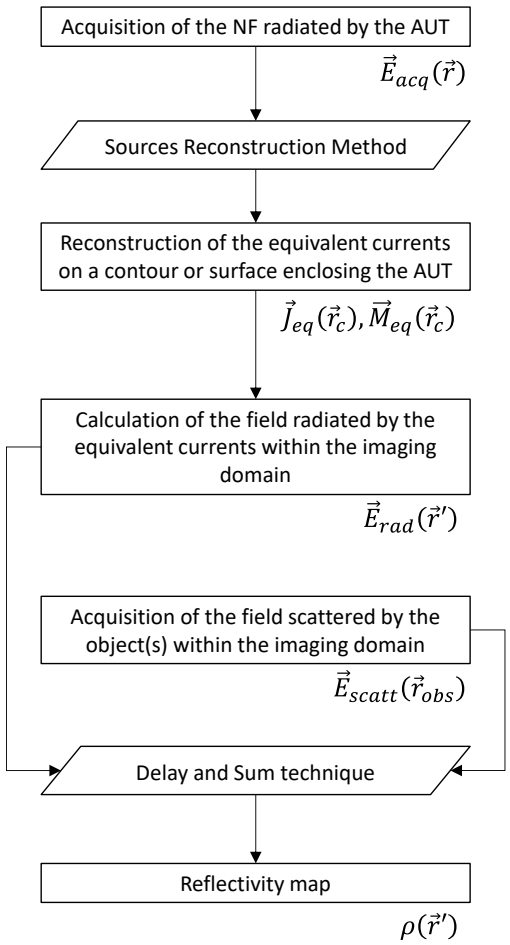

Fig. 4. Flowchart of the inverse scattering technique that uses the electric field radiated by the Tx / Rx antennas.

Given the scattered field acquired in the observation domain ($\vec{E}_{scatt}(\vec{r}_{obs})$) together with the field radiated by the equivalent currents in the imaging domain ($\vec{E}_{rad,OEWG}(\vec{r}')$), the modified backpropagation method (Eq. (9)) is applied. The recovered reflectivity is plotted in Fig. 5 (b). Now, the targets are imaged at their actual position. Besides, the metallic target located at x = 38 cm, y = -26 cm is better imaged.

A video illustrating the methodology described in Section III.A and Section III.B is provided as a supplementary file named "videoImaging.mp4".

C. Impact of the geometry and electric size of the problem

This section is aimed at providing an overview of the influence of the geometry and electric size of the problem on the accuracy of the backpropagation technique without and with the use of the radiation pattern of the Tx and Rx antennas. Two different sets of targets, with smooth and sharp contours, will be considered. And for each set of targets, two different distances between the targets and the scattered field observation domain will be analyzed.

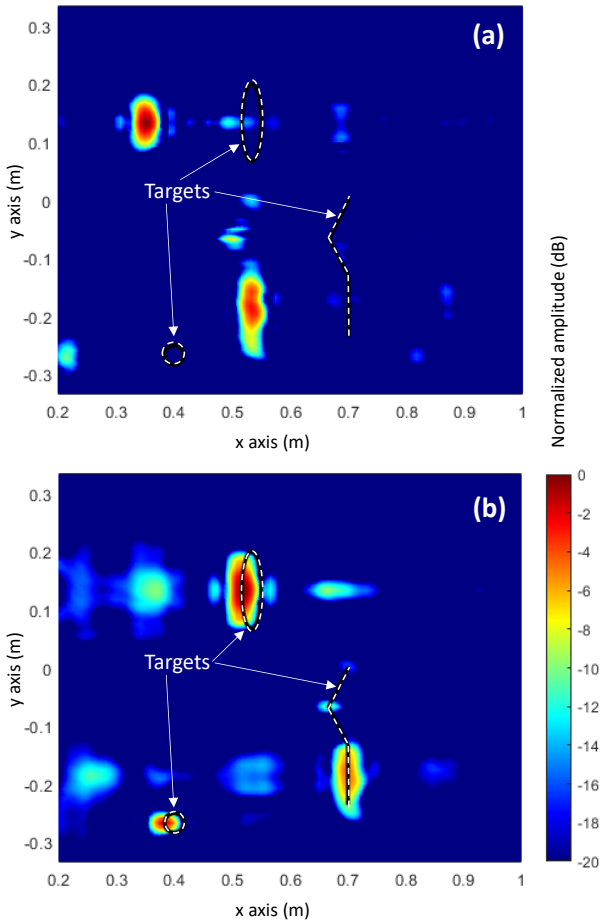

Fig. 5. Reflectivity image. (a) Backpropagation method considering FF approach. (b) Backpropagation method considering the field radiated by the equivalent currents-based model of the antennas.

The imaging setup is the same as in Section III.B, adding a

6-GHz frequency band above and below the 12-18 GHz frequency band to modify the electric size of the imaging problem while keeping the physical size of the targets and the Tx/Rx antennas. Again, a monostatic configuration is considered.

The parameters of each scenario for the different working frequency bands are summarized in Table I and Table II.

Imaging results for the first set of targets (the ones with smooth contours), are depicted in Fig. 6. A summary of the analysis of the reflectivity images of Fig. 6 is provided in the last two rows of Table I.

The second example consists of a single metallic target with a sawtooth profile, similar to the one chosen in [21] for validation purposes. Reflectivity images are plotted in Fig. 7, and the analysis of the imaging results is summarized in Table II.

results corresponding to the backpropagation technique with the FF approach appear shifted with respect to the true position of the targets. Like in the results plotted in in Fig. 5 (a), this is due to the differences between the phase of the FF approach and the true phase pattern of the OEWG antenna (Fig. 2).

TABLE I

DESCRIPTION OF THE SCENARIO AND ANALYSIS OF THE RESULTS SHOWN IN FIG. 6.

Frequency	6 – 12 GHz (f_c = 9 GHz)	12 – 18 GHz (f_c = 15 GHz)	18 – 24 GHz (f_c = 21 GHz)
OEWG FF distance, $r_{FF}=2(D_{OEWG})^2/\lambda$	5.4 cm (1.6λ at f_c) (33.3 cm for $r_{FF} >> \lambda$ at f_c)	9 cm (4.5λ at f_c) (20 cm for $r_{FF} >> \lambda$ at f_c)	12.6 cm (8.8λ at f_c) (16.7 cm for $r_{FF} >> \lambda$ at f_c)
OEWG – target distance (at f_c)	40 cm: 12 λ 80 cm: 24 λ	40 cm: 20 λ 80 cm: 40 λ	40 cm: 28 λ 80 cm: 56 λ
Results considering the FF approach of the phase term	The targets are imaged (a,c).	At 40 cm (e,i) the target placed in front of the bent plate is not well imaged. At 80 cm (g,k), the targets are well imaged.	
Results considering the field radiated by the equivalent model of the OEWG	Barely imaging of the targets (b,d). Presence of clutter in (d).	At 40 cm (f,j), the bent plate is better imaged than in the FF approach (e,i). At 80 cm (h,l), results are similar to the FF approach (g,k).	

The letters in brackets refer to the corresponding subplot in Fig. 6.

From the analysis of the results presented in Fig. 6 and Fig. 7, the following conclusions can be extracted: only when the targets are far from the Tx/Rx antennas of the imaging system (in terms of electric distance), the incident field illuminating the targets can be approached by a spherical wave. In this case, the DAS imaging algorithm with the FF approach of the phase term performs similarly to the modified DAS presented in this contribution. In the examples presented in Fig. 6 and Fig. 7, 40 λ is the minimum distance between the Tx/Rx OEWG antenna and the targets at which the FF approach can be considered sufficiently accurate for imaging purposes.

There is also a low-frequency limit, observed particularly well in the case of the sawtooth-like target (Fig. 7), where none of the backpropagation methods was able to image the target in the 6-12 GHz frequency band. The reason is the insufficient lateral or cross-range resolution, which is given by the electric size of the observation domain. In microwave imaging systems, the lateral or cross-range resolution (Δr) is given by: $\Delta r = r_{target}\ \lambda / L_{obs}$, where r_{target} is the distance between the target and the observation domain, λ is the wavelength at the center frequency of the working frequency band (f_c), and L_{obs} is the length of the observation domain (L_{obs} = 60 cm for the examples presented in Section III). Thus, for the 6-12 GHz frequency band, the cross-range resolution is Δr = 2.2 cm for r_{target} = 40 cm, and Δr = 4.4 cm for r_{target} = 80 cm.

On the other hand, the cross-range resolution improves more than twice for the 18-24 GHz frequency band (Δr = 1 cm for r_{target} = 40 cm, and Δr = 1.9 cm for r_{target} = 80 cm), enabling accurate imaging of the targets.

To sum up, the backpropagation technique considering the field radiated by the Tx/Rx antennas is suitable for those cases where the FF approach of the phase term is not accurate enough (that is, the actual field illuminating the target cannot be modelled using an spherical wave). This is the case when the targets to be imaged are close to the Tx/Rx antennas.

TABLE II

DESCRIPTION OF THE SCENARIO AND ANALYSIS OF THE RESULTS SHOWN IN FIG. 7.

Frequency	6 – 12 GHz (f_c = 9 GHz)	12 – 18 GHz (f_c = 15 GHz)	18 – 24 GHz (f_c = 21 GHz)
Approximate size of the target	12 λ at f_c	20 λ at f_c	28 λ at f_c
Results considering the FF approach of the phase term	The profile cannot be inferred (a,c).	Targets are better imaged at 80 cm (g) than at 40 cm (e).	The profile cannot be inferred at 40 cm (i).
Results considering the field radiated by the equivalent model of the OEWG	Profile barely inferred (b,d). Presence of clutter.	At 80 cm (h), results are similar to the FF approach (g).	At 80 cm (l), results are similar to the FF approach (k).
	High reflectivity values at the sharp edges of the profile due to diffraction effects (especially at 40 cm: (f) and (j)). This phenomenon is intrinsic to the geometry of the target, and is more noticeable when directive Tx/Rx antennas are used.		

The letters in brackets refer to the corresponding subplot in Fig. 7.

The OEWG FF distance and the OEWG – target distance are the same as in Table I.

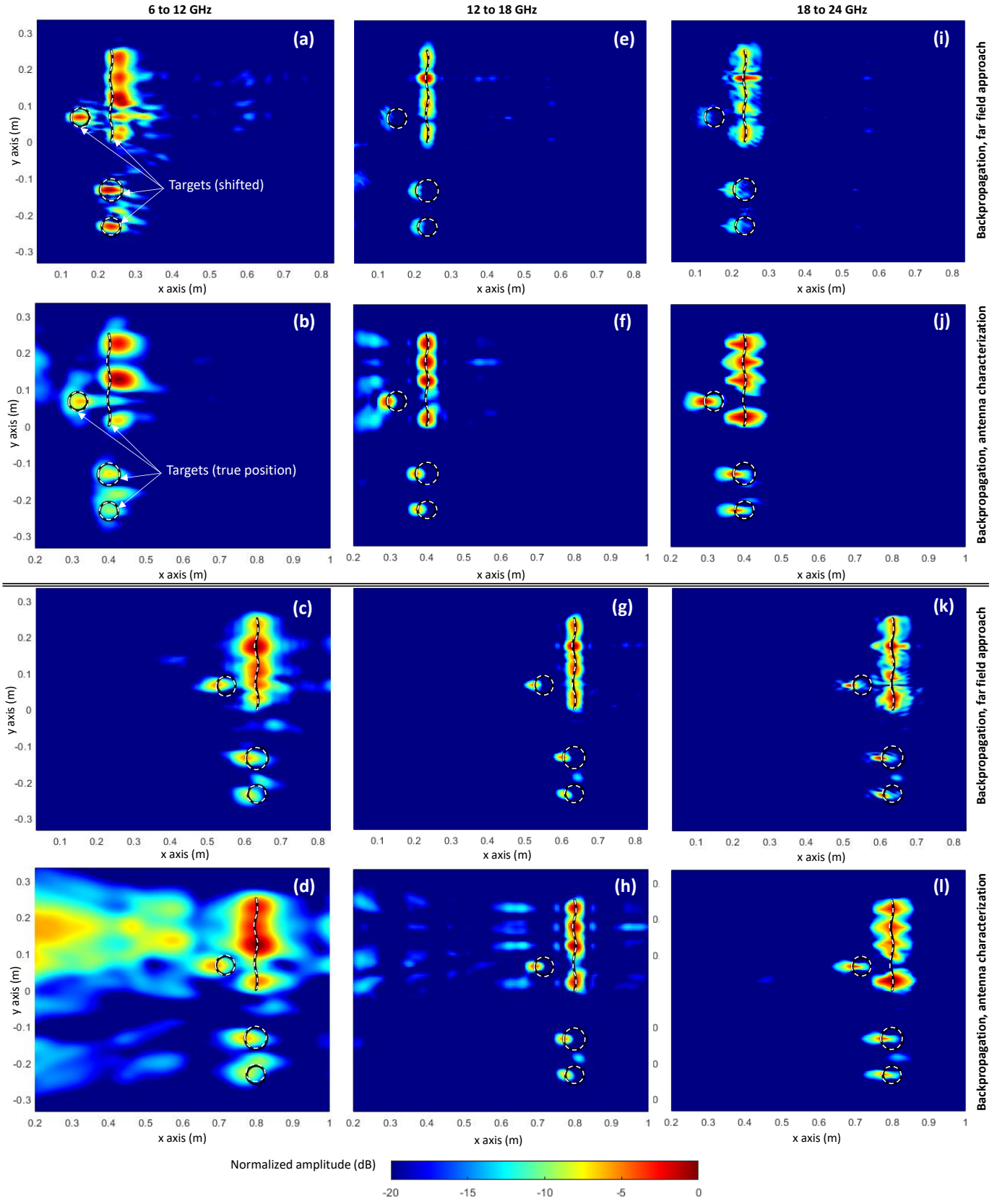

Fig. 6. Reflectivity images for circular targets and a slightly bent plate. (a)-(d) Frequency range: 6 to 12 GHz. (e)-(h) Frequency range: 12 to 18 GHz. (i)-(l) Frequency range: 18 to 24 GHz. Two top rows: targets placed at x = 40 cm. Two bottom rows: targets placed at x = 80 cm. First and third rows: results for backpropagation method considering the FF approach. Second and fourth rows: results for the backpropagation method considering the field radiated by the equivalent currents-based model of the antennas.

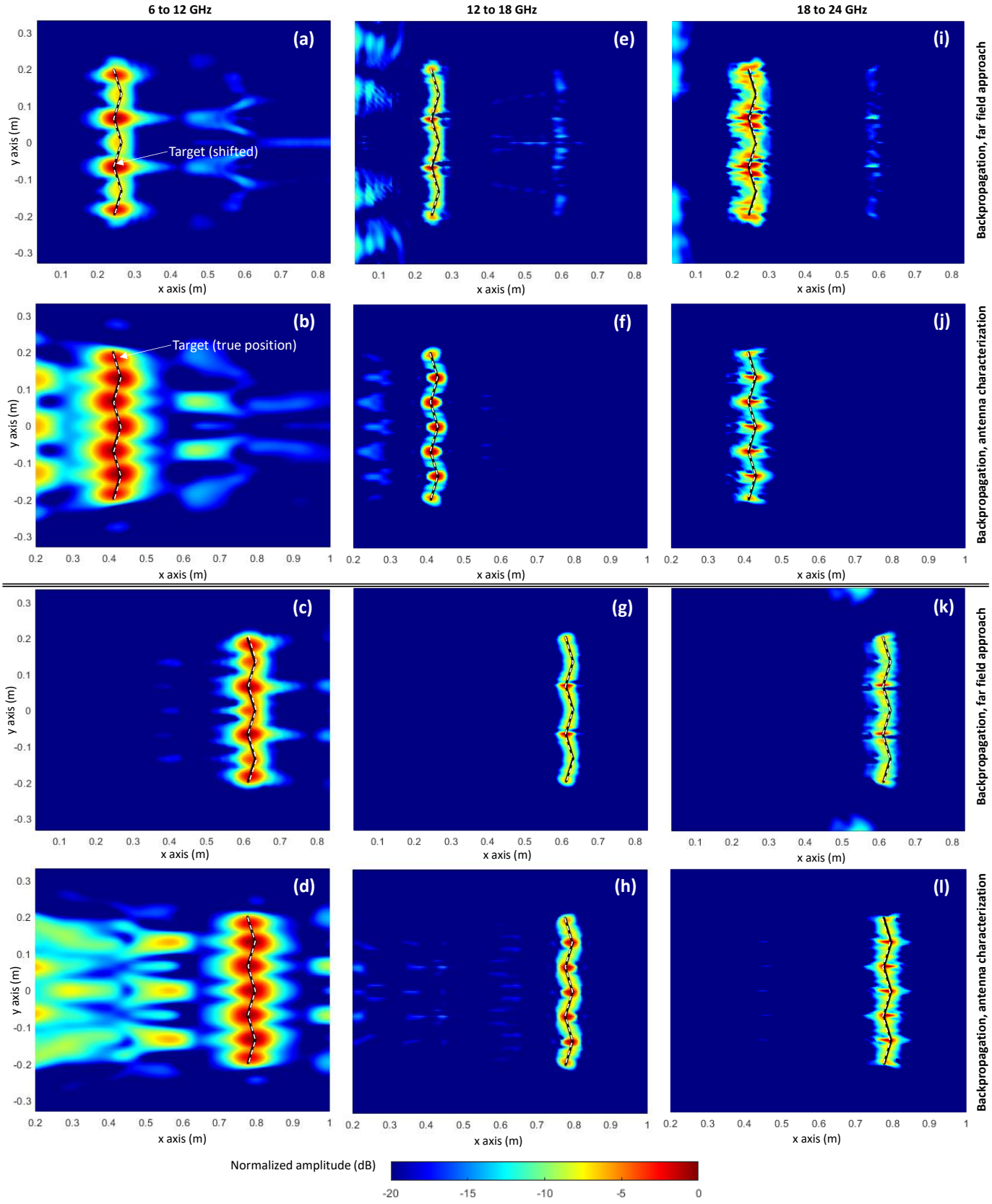

Fig. 7. Reflectivity images for the sawtooth-like target. (a)-(d) Frequency range: 6 to 12 GHz. (e)-(h) Frequency range: 12 to 18 GHz. (i)-(l) Frequency range: 18 to 24 GHz. Two top rows: target placed at x = 40 cm. Two bottom rows: target placed at x = 80 cm. First and third rows: results for backpropagation method considering the FF approach. Second and fourth rows: results for the backpropagation method considering the field radiated by the equivalent currents-based model of the antennas.

D. Analysis of the computational cost

The computational cost of the DAS backpropagation technique is proportional to the number of discrete frequencies in which the frequency band is divided (M_f), the number of observation points $\vec{r}_{obs}$ where the scattered field is acquired (N), and the points in which the imaging domain $\vec{r}'$ is discretized (M). The computational cost of the DAS technique implemented in this contribution is O(M_f N M).

In electrically large imaging problems, the number of points in the observation domain and in the imaging domain will be within the same order of magnitude, that is, $N \approx M$. Under this assumption, the computational cost is O(M_f N^2).

The introduction of the radiation pattern of the Tx and Rx antennas requires an additional step, which is the calculation of the field radiated by the Tx and Rx antennas in all the M points of the imaging domain. If the equivalent currents that characterize the Tx and Rx antennas are discretized into P elements, then, the computational cost of the modified DAS will be O(M_f N M P).

Although the calculation time of the modified DAS is greater, by a factor of P, than the DAS based on the FF approach, the asymptotic behavior with the electric size of the imaging problem does not scale up. The reason is that the electric size of the Tx and Rx antennas will be the same regardless of the electric size of the imaging problem (that is, P will remain the same). Consequently, for electrically large imaging problems, $N \approx M$, with $N >> P$ and $M >> P$. Thus, the resulting computational cost is O(M_f N^2), which is the same as for the conventional DAS backpropagation technique.

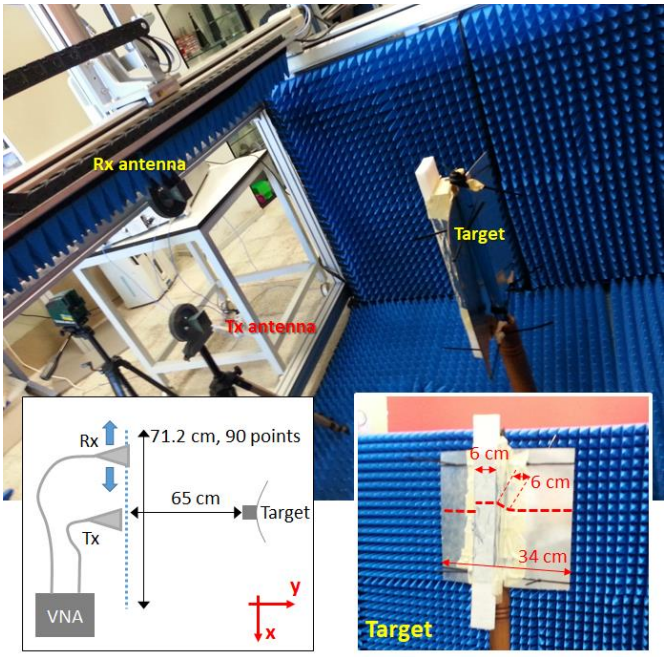

Fig. 8. Picture of the multistatic imaging setup. Lower left plot: scheme of the imaging setup. Lower right plot: picture of the metallic target.

IV. Experimental Validation

The backpropagation imaging technique presented in this contribution has been validated with measurements considering monostatic and multistatic architectures.

A. Multistatic imaging

A picture of the measurement setup is shown in Fig. 8. It consists of a Tx antenna placed at a fixed position and a Rx antenna mounted onto a robotic arm [22] that moves along x axis as shown in Fig. 8. The working frequency band ranges from f = 12 GHz to f =18 GHz, sampled every 150 MHz. The linear aperture for the Rx antenna is 71.2 cm, discretized every 8 mm (approximately λ/2 at 18 GHz). The Object Under Test (OUT) is a bent metallic surface with a rectangular target attached to it. The OUT exhibits translation symmetry along the vertical axis (z axis). The distance between the OUT and the Tx and Rx antennas is 65 cm (32.5 λ at f_c). Both the Tx and Rx antennas are Standard Gain Horn (SGH) antennas, which are connected to a Vector Network Analyzer (VNA).

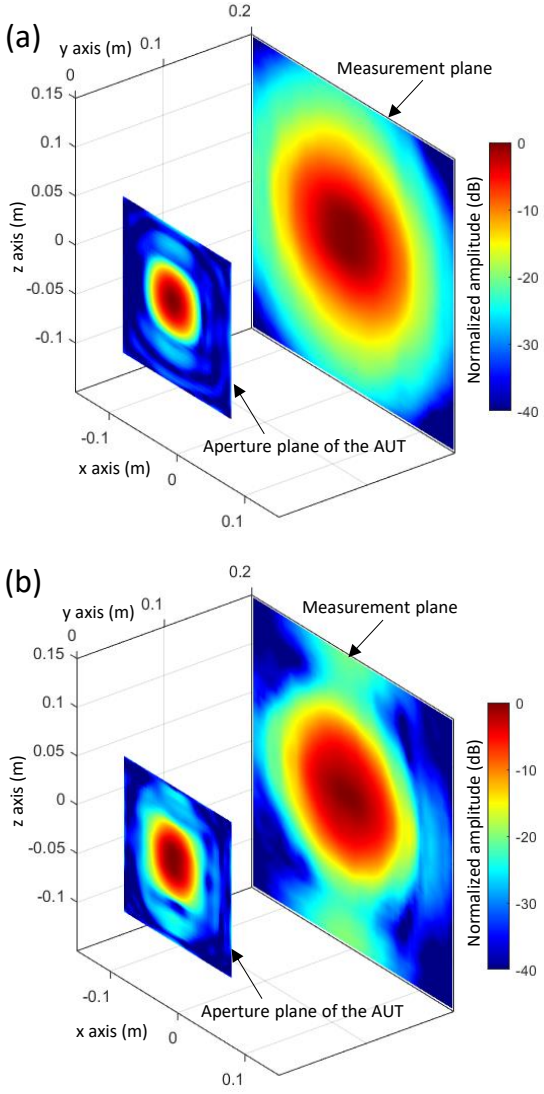

Fig. 9. Measured NF of the AUT (E_y component) and equivalent currents (M_x component) reconstructed on the antenna aperture plane (z = 0 m). (a) f = 12 GHz. (b) f = 18 GHz.

First, the electric field radiated by one of the two SGHs is characterized. The measurement domain is a 30 cm x 30 cm plane located 20 cm in front of the SGH aperture plane, which is within the near field (NF) region of the SGH (the SGH size is D_{SGH} = 12 cm, and thus, for f_c = 15 GHz, the FF distance is $r_{FF} = 2(D_{SGH})^2 / \lambda$ = 1.4 m). The amplitude of the field radiated by the SGH at 12 GHz and 18 GHz is depicted in Fig. 9 (a) and Fig. 9 (b), respectively.

From the measured NF, an equivalent magnetic currents distribution is reconstructed on the SGH aperture plane (also depicted in Fig. 9).

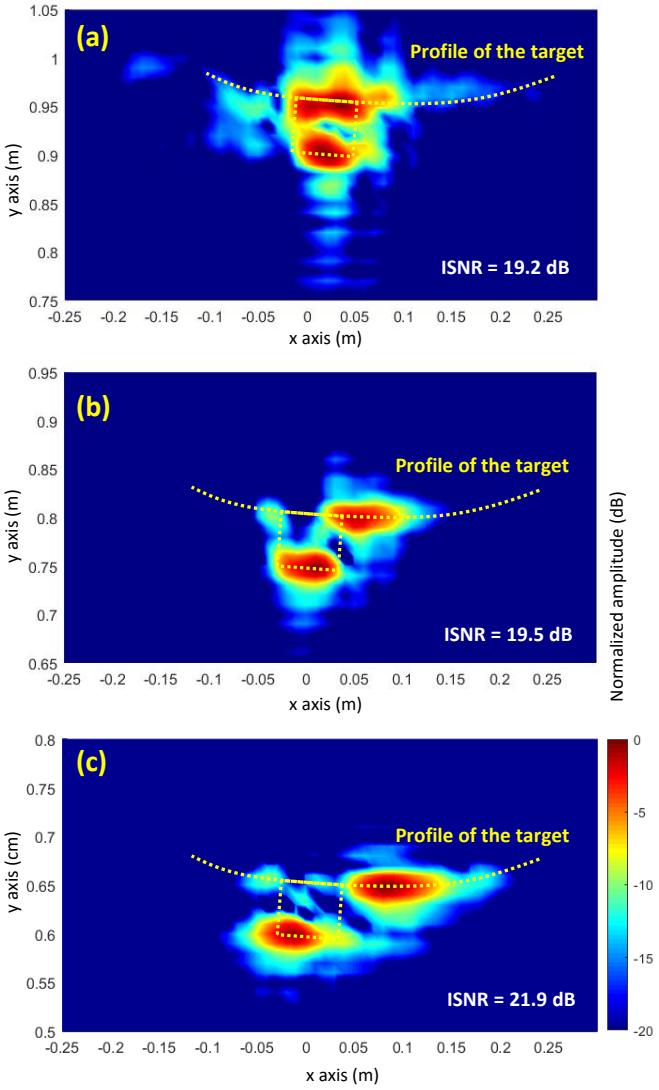

Fig. 10. Reflectivity image. (a) Backpropagation method considering the FF approach. (b) Backpropagation method considering the field radiated by the equivalent currents-based model of the Tx antenna. (c) Backpropagation method considering the field radiated by the equivalent currents-based model of the Tx and Rx antennas.

Taking advantage of the translation symmetry of the OUT, the imaging domain is a 50 cm x 30 cm plane located at the same position in the *z* axis as the linear aperture where the scattered field is measured. First, the DAS algorithm for a multistatic configuration (Eq. (2)) is applied. The recovered reflectivity is shown in Fig. 10 (a), where it is observed that, although the reflection on the flat and bent metallic surfaces are identified, the cross-section of the OUT is not properly retrieved. In particular, the echo on the bent metallic surface should not appear at the position observed in Fig. 10 (a), that is, behind the rectangular target, because this section of the bent target is not illuminated by electromagnetic waves.

Next, the reconstructed equivalent magnetic currents are used to compute the field radiated by SGH in the imaging domain, so that the FF approach of the phase in the DAS algorithm is replaced by the phase of the field radiated by the equivalent currents. Fig. 10 (b) shows the recovered reflectivity when only the phase of the field radiated by the Tx SGH is considered, while keeping the FF approach for the Rx SGH. Now, the cross-section of the OUT is properly recovered. Finally, if the phase of the field radiated by the Rx SGH is also added (Eq. (9)), the recovered reflectivity fits the true profile of the OUT (Fig. 10 (c)).

To provide a quantitative measure of the reflectivity images, the Image Signal to Noise Ratio (ISNR) is provided. The definition of the ISNR can be found in Eq. (15) of [23]. In this example, the highest ISNR value corresponds to the case where the fields of the Tx and Rx antennas are considered in the backpropagation method (Fig. 10 (c)).

B. Monostatic imaging

A monostatic imaging configuration is considered for the second measurement-based validation example. In this example, the Tx and Rx are two Vivaldi antennas working in the 12 GHz to 18 GHz frequency band. A picture of the Vivaldi antenna measurement setup is shown in Fig. 11.

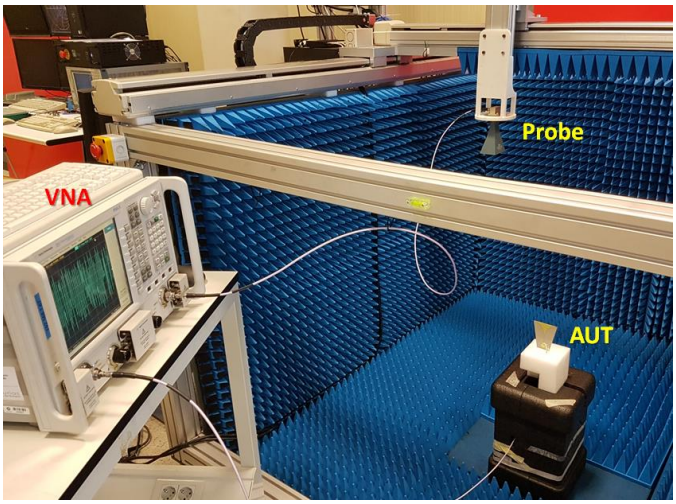

Fig. 11. Measurement of the Vivaldi antenna used in the imaging setup (AUT in the picture). The probe antenna is a standard gain horn (SGH) antenna.

Similarly to the example presented in Section III.A, the field radiated by the Vivaldi antennas has been measured on a plane located 40 cm above the antenna, using an SGH as a probe. In this case, the field radiated by the Vivaldi antenna has been acquired in its NF region (the size of the Vivaldi antenna is

$D_{Vivaldi}$ = 10 cm, and thus, for f_c = 15 GHz, the FF distance is r_{FF} = 2($D_{Vivaldi}$)^2 / λ = 1 m). The amplitude of the measured field is depicted in Fig. 12.

Next, an equivalent currents distribution is reconstructed on the aperture plane of the Vivaldi antenna (depicted at the bottom of Fig. 12), then using these currents to compute the field radiated by the Vivaldi antenna in the imaging domain.

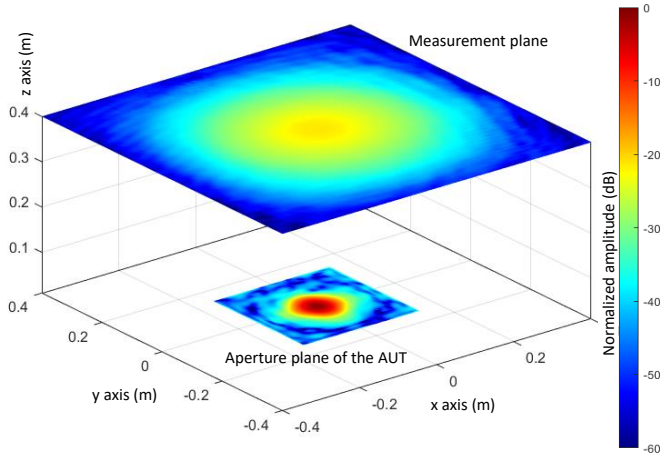

Fig. 12. NF radiated by the Vivaldi antenna acquired on an 80 cm x 80 cm plane placed 40 cm above the Vivaldi antenna aperture plane. The equivalent currents reconstructed on the antenna aperture plane (z = 0 m) are also depicted. f = 12 GHz.

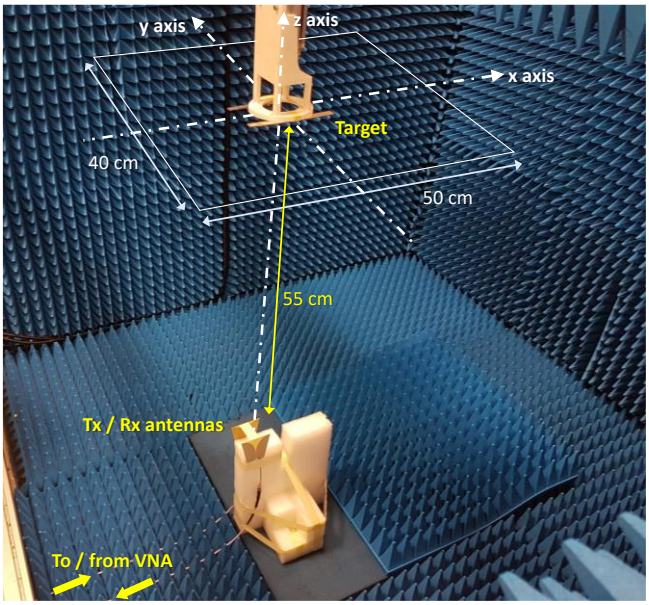

Fig. 13. Picture of the monostatic imaging setup. For the sake of simplicity, the Tx and Rx Vivaldi antennas are fixed, and the target is mounted on the robotic arm of the XYZ measurement table.

Two parallel 15-cm long metallic bars, spaced 10 cm along y axis, have been selected as OUT. A picture of the OUT and the monostatic imaging setup is shown in Fig. 13. For the sake of simplicity, as well as to minimize phase errors due to cable bends, the Tx and Rx antennas are fixed, and the OUT is attached to a robotic arm that moves on an XY plane parallel to the Tx/Rx antennas aperture plane. The field scattered by the OUT has been acquired on a 50 cm x 40 cm domain discretized every 5 mm, thus resulting in 8181 acquisition points. The distance between the OUT and the Tx and Rx Vivaldi antennas is 55 cm (27.5 λ at f_c).

The reflectivity reconstructed in the XY plane is plotted in Fig. 14. The result for conventional DAS (Eq. (1)) is depicted in Fig. 14 (a), and the result for the modified DAS considering the phase of the Tx and Rx antennas is plotted in Fig. 14 (b). It can be observed that the modified backpropagation technique provides a sharper image that fits best the profile of the two metallic bars. This improvement is supported by the ISNR values obtained for the reflectivity images, as the ISNR of Fig. 14 (b) is greater than the ISNR of Fig. 14 (a).

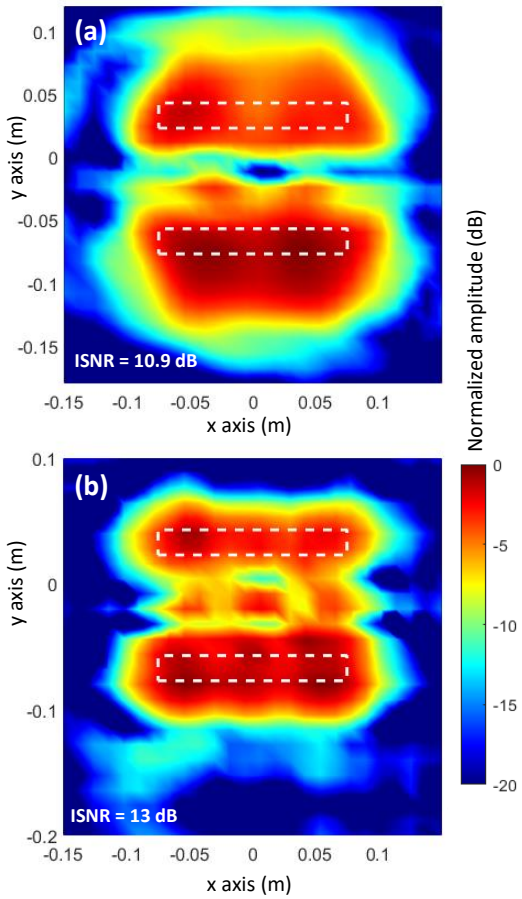

Fig. 14. Reflectivity image recovered on the XY plane. (a) Backpropagation method considering the FF approach. (b) Backpropagation method considering the field radiated by the equivalent currents-based model of the Tx and Rx antennas.

C. Application in a realistic scenario

In order to illustrate the performance of the method in a realistic scenario, a set of measurements taken with a portable monostatic imaging system implemented for teaching a radar course has been selected. A picture of the setup is shown in Fig. 15: it consists of a pair of horn antennas connected to a VNA, working in the 4-7 GHz frequency band. For these antennas, the FF distance is r_{FF} = 2(D_{horn})^2 / λ = 3.2 m at f_c = 5.5 GHz. The

VNA and the horn antennas are mounted on top of a wooden cart that can be manually moved to collect measurements at different positions. The objects in the imaging scenario are a cardboard panel placed 1.5 m (27.5 λ at f_c) far from the Tx/Rx antennas, and two metallic bars located 75 cm behind the panel (that is, 41.3 λ from the Tx/Rx antennas). The scattered field is collected in a linear domain ranging from x = -37.5 cm to x = 37.5 cm, and sampled every 2.5 cm.

Reflectivity images are depicted in Fig. 16, where Fig. 16 (a) corresponds to the backpropagation technique considering the FF approach, and Fig. 16 (b) corresponds to the modified DAS considering the radiation pattern of the horn antennas. In this example, the main difference is that the cardboard panel (the target closest to the Tx/Rx antennas) is best imaged with the latter method. Also, the ISNR improves when the radiation pattern of the horn antennas is considered.

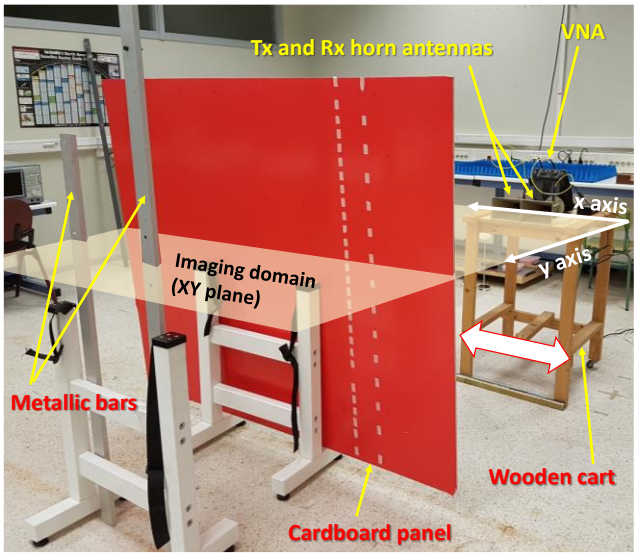

Fig. 15. Picture of the portable monostatic imaging setup and the targets under test.

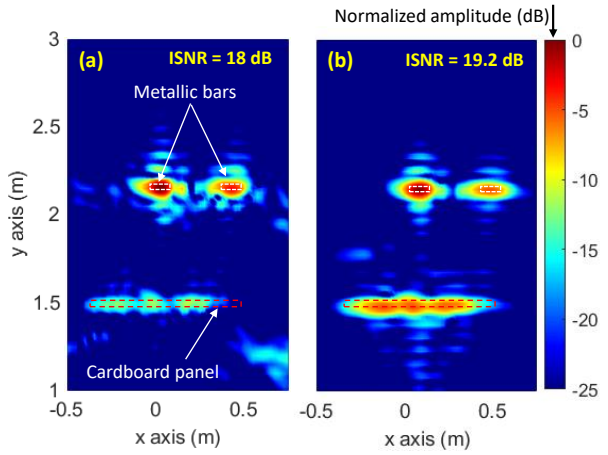

Fig. 16. Reflectivity images obtained with the portable imaging setup (4-7 GHz frequency band). (a) Backpropagation method considering the FF approach. (b) Backpropagation method considering the field radiated by the equivalent currents-based model of the Tx and Rx horn antennas.

V. Conclusion

This contribution has presented a method that takes into account the field radiated by the Tx and Rx antennas to improve the DAS backpropagation technique. Results shown in this contribution support the fact that an accurate characterization of the fields radiated by the Tx and Rx antennas of the imaging system results in better focused microwave images.

From a technical complexity point-of-view, the proposed methodology requires only one measurement of the field radiated by Tx and Rx antennas to obtain an electromagnetic model of these antennas. Besides, once this characterization is conducted, it can be reused in any imaging setup that uses these antennas.

It must be pointed out that even backpropagation techniques based on the FF approach of the propagation term require a calibration stage. This calibration consists of placing one or more reference targets within the imaging domain to correct the offset distance in the reflectivity images provided by the imaging system. Thus, the use of the actual field radiated by the Tx and Rx antennas avoids the need for calibration targets.

The methodology presented in this contribution is of special interest for portable scanners [24],[25], where the distance between the scanning device and the objects to be inspected can be small enough to require precise modeling of the fields radiated by the Tx and Rx antennas of the scanner to obtain focused microwave images.

The proposed technique is a trade-off between accurate but computationally expensive imaging methods (e.g. model-based techniques [26], tomographic approach [27]), and fast imaging techniques based on FF approaches (DAS [17]-[19], Phase-Shift Migration [28]).

References

[1] S. S. Ahmed, "Microwave Imaging in Security — Two Decades of Innovation," *IEEE Journal of Microwaves*, vol. 1, no. 1, pp. 191-201, Jan. 2021, doi: 10.1109/JMW.2020.3035790.

[2] S. Kharkovsky, A. C. Ryley, V. Stephen and R. Zoughi, "Dual-Polarized Near-Field Microwave Reflectometer for Noninvasive Inspection of Carbon Fiber Reinforced Polymer-Strengthened Structures, "*IEEE Transactions on Instrumentation and Measurement*, vol. 57, no. 1, pp. 168-175, Jan. 2008, doi: 10.1109/TIM.2007.909497.

[3] B. Wu, Y. Gao, J. Laviada, M. T. Ghasr and R. Zoughi, "Time-Reversal SAR Imaging for Nondestructive Testing of Circular and Cylindrical Multilayered Dielectric Structures," *IEEE Transactions on Instrumentation and Measurement*, vol. 69, no. 5, pp. 2057-2066, May 2020, doi: 10.1109/TIM.2019.2918371.

[4] J. S.Lee, C. Nguyen and T. Scullion, "A novel, compact, low-cost, impulse ground-penetrating radar for nondestructive evaluation of pavements," *IEEE Transactions on Instrumentation and Measurement*, vol. 53, no. 6, pp. 1502-1509, Dec. 2004, doi: 10.1109/TIM.2004.827308.

[5] J. R. Gallion and R. Zoughi, "Millimeter-Wave Imaging of Surface-Breaking Cracks in Steel With Severe Surface Corrosion," *IEEE Transactions on Instrumentation and Measurement*, vol. 66, no. 10, pp. 2789-2791, Oct. 2017, doi: 10.1109/TIM.2017.2735658.

[6] T. Sleasman, M. F. Imani, O. Yurduseeeven, K. P. Trofatter, V. R. Gowda, D. L. Marks, J. N. Gollub and D. R. Smith, "Near Field Scan Alignment Procedure for Electrically Large Apertures," *IEEE Transactions on Antennas and Propagation*, vol. 65, no. 6, pp. 3257-3262, June 2017, doi: 10.1109/TAP.2017.2691465.

[7] C. Liu, M. T. A. Qaseer and R. Zoughi, "Influence of Antenna Pattern on Synthetic Aperture Radar Resolution for NDE Applications," *IEEE Transactions on Instrumentation and Measurement*, vol. 70, pp. 1-11, 2021, Art no. 8000911, doi: 10.1109/TIM.2020.3026122.

[8] M. González-Díaz, M. García-Fernández, Y. Álvarez-López and F. Las-Heras, "Improvement of GPR SAR-Based Techniques for Accurate Detection and Imaging of Buried Objects," *IEEE Transactions on Instrumentation and Measurement*, vol. 69, no. 6, pp. 3126-3138, June 2020, doi: 10.1109/TIM.2019.2930159.

[9] J. Wittemeier, B. Sievert, M. Dedic, D. Erni, A. Rennings and N. Pohl, "The Impact of Group Delay Dispersion on Radar Imaging With Multiresonant Antennas," *IEEE Microwave and Wireless Components Letters*, doi: 10.1109/LMWC.2021.3128281.

[10] M. García-Fernández, Y. Álvarez López, A. De Mitri, D. Castrillo Martínez, G. Álvarez-Narciandi and F. Las-Heras Andrés, "Portable and Easily-Deployable Air-Launched GPR Scanner," *Remote Sensing*, 2020, 12, 1833, doi: 10.3390/rs12111833.

[11] Y. Alvarez, F. Las-Heras and M. R. Pino, "Reconstruction of Equivalent Currents Distribution Over Arbitrary Three-Dimensional Surfaces Based on Integral Equation Algorithms," *IEEE Transactions on Antennas and Propagation*, vol. 55, no. 12, pp. 3460-3468, Dec. 2007, doi: 10.1109/TAP.2007.910316.

[12] Y. Alvarez Lopez, F. Las-Heras Andres, M. R. Pino and T. K. Sarkar, "An Improved Super-Resolution Source Reconstruction Method," *IEEE Transactions on Instrumentation and Measurement*, vol. 58, no. 11, pp. 3855-3866, Nov. 2009, doi: 10.1109/TIM.2009.2020847.

[13] J. L. Araque Quijano and G. Vecchi, "Improved-Accuracy Source Reconstruction on Arbitrary 3-D Surfaces," *IEEE Antennas and Wireless Propagation Letters*, vol. 8, pp. 1046-1049, 2009, doi: 10.1109/LAWP.2009.2031988.

[14] S. Nounouh, C. Eyraud, A. Litman and H. Tortel, "Quantitative Imaging With Incident Field Modeling From Multistatic Measurements on Line Segments," *IEEE Antennas and Wireless Propagation Letters*, vol. 14, pp. 253-256, 2015, doi: 10.1109/LAWP.2014.2360775.

[15] M. Ostadrahimi, P. Mojabi, C. Gilmore, A. Zakaria, S. Noghanian, S. Pistorius and J. LoVetri, "Analysis of Incident Field Modeling and Incident/Scattered Field Calibration Techniques in Microwave Tomography," *IEEE Antennas and Wireless Propagation Letters*, vol. 10, pp. 900-903, 2011, doi: 10.1109/LAWP.2011.2166849.

[16] C. Narendra, I. Jeffrey and P. Mojabi, "Using the Source Reconstruction Method to Model Incident Fields in Microwave Tomography," *IEEE Antennas and Wireless Propagation Letters*, vol. 16, pp. 46-49, 2017, doi: 10.1109/LAWP.2016.2554059.

[17] V. Perrot, M. Polichetti, F. Varray and Damien Garcia, "So you think you can DAS? A viewpoint on delay-and-sum beamforming," *Ultrasonics*, Volume 111, 2021, 106309, doi: 10.1016/j.ultras.2020.106309.

[18] S. Rost and C. Thomas, "Array seismology: methods and applications," *Reviews of Geophysics*, Vol. 40, No. 3, 27 pages, September 2002. Doi: 10.1029/2000RG000100.

[19] Y. Yang, Z. Chu, L. Shen and Z. Xu, "Functional delay and sum beamforming for three-dimensional acoustic source identification with solid spherical arrays," *Journal of Sound and Vibration*, Vol. 373, pp. 340-359, 2016. Doi: 10.1016/j.jsv.2016.03.024

[20] S. R. Rengarajan and Y. Rahmat-Samii, "The field equivalence principle: illustration of the establishment of the non-intuitive null fields," *IEEE Antennas and Propagation Magazine*, vol. 42, no. 4, pp. 122-128, Aug. 2000, doi: 10.1109/74.868058.

[21] B. Gonzalez-Valdes, Y. Alvarez, J. A. Martinez-Lorenzo, F. Las-Heras and C. M. Rappaport, "On the Combination of SAR and Model Based Techniques for High-Resolution Real-Time Two-Dimensional Reconstruction," *IEEE Transactions on Antennas and Propagation*, Vol. 62, No. 10, pp. 5180-5189, Oct. 2014, doi: 10.1109/TAP.2014.2346203.

[22] A. Arboleya, Y. Álvarez and F. Las-Heras, "Millimeter and submillimeter planar measurement setup," *2013 IEEE Antennas and Propagation Society International Symposium (APSURSI)*, Orlando, USA, 7-13 July 2013, pp. 1-2, doi: 10.1109/APS.2013.6710661.

[23] W. Zhang, M. G. Amin, F. Ahmad, A. Hoorfar, and G. E. Smith, "Ultrawideband impulse radar through-the-wall imaging with compressive *sensing," International Journal on Antennas and Propagation*, vol. 2012, p. 251497, 2012. doi: 10.1155/2012/251497

[24] G. Álvarez-Narciandi, M. López-Portugués, F. Las-Heras and J. Laviada, "Freehand, Agile, and High-Resolution Imaging With Compact mm-Wave Radar," *IEEE Access*, vol. 7, pp. 95516-95526, 2019, doi: 10.1109/ACCESS.2019.2929522

[25] J. T. Case, M. T. Ghasr and R. Zoughi, "Nonuniform Manual Scanning for Rapid Microwave Nondestructive Evaluation Imaging," *IEEE Transactions on Instrumentation and Measurement*, vol. 62, no. 5, pp. 1250-1258, May 2013, doi: 10.1109/TIM.2012.2220034.

[26] R. O. Mays, N. Behdad and S. C. Hagness, "Array Sensitivity for Model-Based Microwave Breast Imaging," *IEEE Transactions on Antennas and Propagation*, vol. 65, no. 6, pp. 2958-2965, June 2017, doi: 10.1109/TAP.2017.2688800.

[27] R. Persico, F. Soldovieri and G. Leone, "A Microwave Tomographic Imaging Approach for Multibistatic Configuration: The Choice of the Frequency Step," *IEEE Transactions on Instrumentation and Measurement*, vol. 55, no. 6, pp. 1926-1934, Dec. 2006, doi: 10.1109/TIM.2006.884346.

[28] G. Yang, C. Li, H. Gao and G. Fang, "Phase Shift Migration With SIMO Superposition for MIMO-Sidelooking Imaging at Terahertz Band," *IEEE Access*, vol. 8, pp. 208418-208426, 2020, doi: 10.1109/ACCESS.2020.3017617.